Microfluidics and Nanofluidics manuscript No.
(will be inserted by the editor)

The fluidic resistance of an array of obstacles and a method for improving boundaries in Deterministic Lateral Displacement arrays

David Inglis · Rohan Vernekar · Timm Krüger · Shilun Feng

Received: date / Accepted: date

Abstract Deterministic Lateral Displacement (DLD) is a microfluidic method of separating particles by size. DLD relies on precise flow patterns to deliver high-resolution particle separation. These patterns determine which particles are displaced laterally, and which follow the flow direction. Prior research has demonstrated that the lateral array boundaries can be designed to improve the uniformity of the critical size and hence separation performance. A DLD device with an invariant critical size throughout is yet unknown. In this work we propose a 3D design approach. We first represent the flow through the DLD as a 2D lattice of resistors. This is used to determine the relative flow resistances at the boundaries that will deliver the correct flux patterns. We then use the Lattice Boltzmann Method to simulate fluid flow in a 3D unit cell of the DLD and measure the fluidic resistance for a range or typical dimensions. The results of this work are used to create a new equation for fluidic resistance as a function of post size, post height, and post spacing. We use this equation to determine array geometries that should have the appropriate resistances. We then design and simulate (in COMSOL) complete devices and measure fluid fluxes and first flow-lane widths along the boundaries. We find that the first flow-lane widths are much more uniform than in any devices described previously. This work provides the best method for designing periodic boundaries, and enables narrower, shorter and higher throughput DLD devices.

D.W. Inglis
School of Engineering, Macquarie University, Sydney, Australia
E-mail: david.inglis@mq.edu.au

R. Vernekar
School of Engineering, Institute for Multiscale Thermofluids, University of Edinburgh, Edinburgh EH9 3FB, UK.

T. Krüger
School of Engineering, Institute for Multiscale Thermofluids, University of Edinburgh, Edinburgh EH9 3FB, UK.

S. Feng
School of Electrical and Electronic Engineering, Nanyang Technological University, 639798 Singapore

Keywords Deterministic Lateral Displacement · modelling and simulation · design · flow resistance

1 Introduction

Deterministic Lateral Displacement (DLD) is a microfluidic method of separating particles by size (Huang et al, 2004). In it, particles move through a periodic, 2D array of obstacles at low Reynolds numbers *Re* (see fig. 1). The columns of obstacles are arranged at a small angle θ relative to the average flow direction. Particles larger than a set critical size D_c follow the columns of obstacles, while smaller particles ($< D_c$) follow the average flow direction, due to physical differences in particle-obstacle interactions. More details are provided in two recent DLD reviews (McGrath et al, 2014; Salafi et al, 2019).

DLD relies on precise flow patterns to deliver high performance particle separation. These flow lane patterns marked out by stagnation streamlines, in particular the width of the flow lane adjacent to an obstacle, β, is the principle determinant of the critical particle size ($D_c \approx 2\beta$) (Inglis et al, 2006). Larger particles 'bump' on the obstacles, crossing streamlines while smaller particles stay within their flow lanes. It is understood that finite-sized particles do not necessarily follow streamlines (Doyeux et al, 2011); however, their paths are deterministic in the high Péclet number regime, and a goal for most DLD device designs is to have a consistent critical particle separation size throughout an array.

If the width β is not consistent throughout, bi-modal particle separation will break down. That is, similarly sized particles will be bumped in some regions and not in others, ultimately leading to dispersion and poor separation performance. Vernekar et al (2017) showed that anisotropic permeability of an array can cause local changes to the effective array tilt and therefore changes to the first flow-lane width near the entrance and exit regions of arrays. Pariset et al (2017) demonstrated that the critical particle size varies near the edges of a DLD array and that, if the device is narrow, the critical size over the entire device width is not uniform. Prior to that, Inglis (2009) showed that the lateral array boundaries can be engineered to improve separation performance near the boundaries.

In Inglis (2009), boundaries created by masking a straight microfluidic channel wall onto the obstacle array caused the critical size to be zero in some regions and as much as 170% larger than intended in other areas. The boundary problem was partially solved by growing and shrinking gaps at the boundaries by the square root of the desired flux through them. This solution showed promise in 2D simulations and in experiments with beads much larger than the critical diameter. Feng et al (2017) used a comparable approach and found a similar problem. Beads that are twice the critical size bumped properly everywhere. But beads that are 48% above the critical size stopped bumping when they were within 11 columns of a boundary. The 3D flow pattern was also observed experimentally and showed significant deviations from the ideal one, and one based on 2D designs.

Recently Ebadi et al (2019) proposed a modification to the equations used by Inglis (2009) and Feng et al (2017). Rather than growing or shrinking boundary gaps

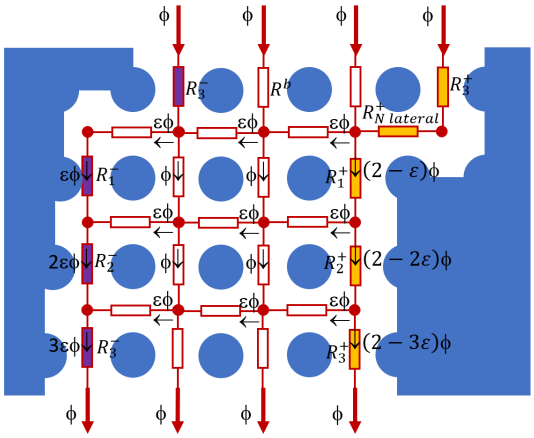

Fig. 1 Schematic of DLD array having a row shift fraction $\varepsilon = 1/N$ with $N = 3$. Resistors are overlaid onto the array. Resistances along the negative boundary are colored purple and along the positive boundary they are yellow. ϕ is the unit of flux entering each vertical gap.

by the square root or cube root of the desired flux, they used 2D simulations to numerically determine the correct power for a range of pillar sizes. Their work shows improved consistency of critical size in 2D simulations, but the worst performing regions still have up to 25% errors in flux.

The boundary problem has not yet been solved, and no solution for 3D devices has ever been proposed. In this work, we model the DLD array as a rectangular lattice of resistors and apply electrical circuit techniques to determine the relative resistance of the fluidic gaps that would deliver the desired flux patterns. At low Reynolds number, fluidic channels behave as linear resistors where the resistance (as in Ohm's law) is defined as the pressure drop along the length of a channel divided by the mass flow rate through that channel. Fluidic resistance therefore has units of $\mathrm{Pa\,s/m^3}$ or $\mathrm{N\,s/m^5}$.

We use the lattice Boltzmann method to model a DLD unit cell and find its resistance. These resistances are fitted to an explicit equation, and this equation, coupled with the circuit analog is used to determine array geometries with the appropriate fluidic gaps. To validate the approach, we simulate complete devices using COMSOL Multiphysics 3.5a and measure fluid transport and first flow-lane widths along the boundaries. Our results are superior compared to all previous boundary treatements.

2 Model of flow through DLD

Fig. 1 shows an example array with a fractional row shift of $\varepsilon = \tan\theta = 1/3$. We shall model each horizontal and vertical gap as a resistor, placing nodes in the open regions. The bulk resistors (white in Fig. 1) are R^b. The left side is the negative boundary ($^-$) because particles are depleted there, these are coloured purple and numbered $n = 1 \ldots N$ (where $N = 3$ in this example). The right side is the positive boundary ($^+$) because particles concentrate here, these are coloured yellow and similarly numbered $n = 1 \ldots N$.

Each vertical white resistor carries one unit of flux ϕ. Each horizontal white resistor carries $\varepsilon\phi$ units of flux. The negative boundary resistors (purple) therefore carry $n\varepsilon\phi$ units of flux. At the positive boundary, the vertical yellow resistors carry $\phi(2-n\varepsilon)$ units of flux.

Using simple circuit analysis, we can determine the resistance values needed to ensure this pattern of currents/fluxes persists at all nodes, including boundary resistances. The negative boundaries resistances are

$$R_n^- = \frac{R^b}{n\varepsilon},$$

and the resistances along the positive boundary are:

$$R_n^+ = \frac{R^b}{2-n\varepsilon}.$$

The N^{th} gap on the positive boundary requires some special treatment. In the bulk, the pressure drop in moving one unit down and one unit left is $R^b(\phi+\varepsilon\phi)$. The flux entering the N^{th} gap at the top right of Fig. 1 must experience the same pressure drop as it moves one unit down and one unit left. Therefore we have

$$\begin{aligned}\phi(R_N^+ + R_{N,\text{lat}}^+) &= \phi R^b(1+\varepsilon),\\ R_N^+ &= R^b(1+\varepsilon) - R_{N,\text{lat}}^+.\end{aligned}$$

$R_{N,\text{lat}}^+$ is normally equal to R^b. This forces $R_N^+ = \varepsilon R^b$. When ε is small, it may not be possible to create a gap with such low resistance. In these cases, we must reduce the value of $R_{N,\text{lat}}^+$. This gives a non-unique solution for the positive boundary where the designer must choose a value of R_N^+ and calculate $R_{N,\text{lat}}^+$, or choose $R_{N,\text{lat}}^+$ then calculate R_N^+.

The result that R_N^+ must be small, whereas the preceding gap has a resistance nearly equal to that in the bulk, is entirely new. However, it is similar to the ad-hoc modifications made to the positive boundary in prior work (Inglis, 2009). The full equation for the resistances along the positive boundary is then

$$R_n^+ = \begin{cases} \frac{R^b}{2-\frac{n\varepsilon}{N}} & n < N, \\ R^b(1+\varepsilon) - R_{N,\text{lat}}^+ & n = N. \end{cases} \tag{1}$$

3 Resistance of arbitrary gap

Now that we have determined the necessary resistances, we must design 3D fluidic gaps (resistors) that match. The resistance between any two nodes in the bulk of the array shown in Fig. 1 can be determined through computational fluid dynamics. We have used lattice Boltzmann (LB) simulations (Krüger et al, 2017) at $\text{Re} < 0.03$ to determine the resistance between two nodes for a range of pillar sizes and array depths (Fig. 2a). The Reynolds number is defined as the average flow velocity times the gap size, divided by the kinematic viscosity. All pillars are cylindrical with $\varepsilon =$

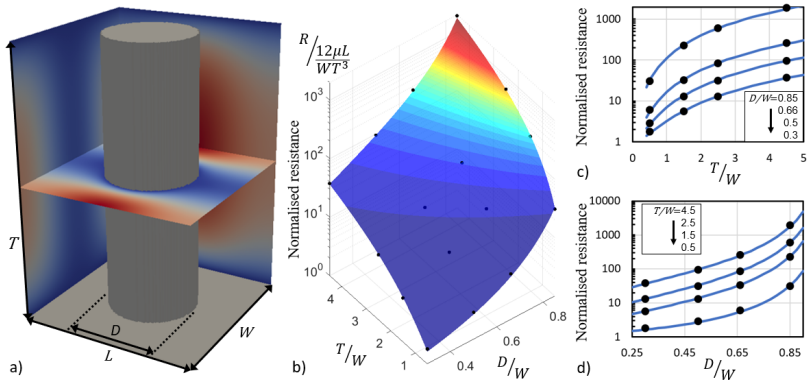

Fig. 2 a) Example simulation domain ($100 \times 100 \times 152\Delta x^3$) used to determine the resistance of a 3D pillar array. D and T are varied, W and L are fixed. Flow is in the direction of L. b) Normalised resistance plotted as a function of normalised thickness (T/W) and pillar diameter (D/W). The normalised resistance is the ratio of actual resistance to the resistance that would be found if the pillar were removed. c)/d) The same data presented as 2D plots. Blue lines represent Eq. (2). Note the logarithmic axis and excellent agreement over three orders of magnitude.

0. We assume that typical values for row shift fraction have a negligible effect on resistance. Width W and length L of a unit cell are equal.

We use the BGK collision operator (with relaxation time set to $1.5\Delta t$ in all simulations where Δt is the time step size). Obstacles and walls are modelled with the half-way bounce-back scheme. The flow is driven by a constant body force, with periodic boundaries for the unit cell. The mesh sizes range from $100 \times 100 \times 52\Delta x^3$ ($T/W = 0.5$) to $100 \times 100 \times 452\Delta x^3$ ($T/W = 4.5$) where Δx is the lattice spacing. The extra 2 lattice units in the z-direction are no-slip boundary nodes. In each case $\Delta x = 0.5\mu$m. To check for mesh invariance, we checked the resistance for a particular geometry at $0.8\times$ and $2\times$ the original mesh density. At twice the mesh density the resistance was reduced by 0.03%, and at a the reduced mesh density the resistance was reduced by 2%.

The resistance values measured from the LB simulations are used to create a new equation for the resistance of a pillar array:

$$R = \frac{12\mu L}{WT^3}\left[1 + a\left(b + \tan\left(\frac{\pi D}{2W}\right)\right)^c \left(\frac{T}{W}\right)^d\right]. \tag{2}$$

W, L, D, and T are defined in Fig. 2a, and μ is the fluid viscosity. a, b, c and d are fitting parameters. The leading term $12\mu L/(WT^3)$ is the resistance for a wide rectangular channel, the planar Poiseuille result. The following terms modulate this resistance as follows. As D approaches W, the gap goes to zero and the tangent function forces the resistance to infinity. The last term modulates the effect of the pillar through the aspect ratio T/W: when T is larger than W, the effect of the pillar on the unit cell's resistance is amplified, and conversely, suppressed when T is less than W.

Fig. 2b and c show the measured resistances as black dots and Eq. (2) as a surface (blue lines). The resistance is normalised by the planar Poiseuille result $12\mu L/(WT^3)$,

so a value of 1 means the pillar has no effect on resistance. Fitting parameter values were determined by minimising the sum of the squares of the *relative* error. Because the data covers around three orders of magnitude, it is essential to use relative, rather than absolute error. Values of $a = 1.702$, $b = 0.600$, $c = 2.682$, $d = 1.833$, give an excellent fit over the entire range used: $0.3 \leq D/W \leq 0.9$, $0.5 \leq T/W \leq 4.5$. The standard deviation of error is 5%, and the normalised root mean square of percent error is 1.4%. The maximum error is 10%. These fitting parameters do not appear to have any physical significance, and we do not expect the equation to be a good fit for ratios of D/W and T/W that are outside of the range used here.

Eq. (2) is also useful for predicting device-level throughput and resistance when designing microfluidic devices that use pillar arrays including DLD and immunocapture devices (Nagrath et al, 2007; Gleghorn et al, 2010). Prior experimental efforts to measure the resistance of pillar arrays highlighted that models based on porous media do not accurately predict resistance of pillar arrays (Gunda et al, 2013).

4 Device Design

In the layout of a DLD device it is not practical to adjust the pillar diameter, or the cell length, but only the gap size. To proceed, we assume Eq. (2) is valid for unit cells where W is not strictly equal to L, but similar. To test our design approach we have used Eq. (1) to determine boundary resistances for three DLD designs. Eq. (2) cannot be explicitly solved for W. Therefore, to determine W for a given R (D, T, and L are fixed), we use the MATLAB function 'fzero', which uses numeric interpolation of a function.

Three designs are shown in Fig. 3. The row shift ε for the three designs are $1/32$, $1/12$, and $1/8$. The depth ranges from shallow ($T/W = 0.75$) to deep ($T/W = 2$), and the post size is 0.5 and 0.65 times the pitch (D/W). The design presented in the second row of Fig. 3 has a slightly asymmetric gap, a useful modification described nicely by Zeming et al (2016). The pillar is elliptical giving a lateral gap of 20 μm and an axial or downstream gap of 17 μm.

Fig. 3 compares the proposed boundary treatment to the square root method (Inglis, 2009), and the cube root method (Feng et al, 2017). The proposed method lies in between the two prior solutions everywhere except at the N^{th} gap on the positive boundary. Here, the pressure drop caused by a full unit of flux move laterally is so large that the N^{th} lateral gap must be made very large. By making it large, the the combined pressure drop can be equal to the bulk array pattern. By including the lateral resistances, the proposed treatment identifies this problem, and makes a significant departure from all prior work.

Fig. 3f) shows the gaps for the positive boundary of an array with $\varepsilon = 8$, a post of 13 μm, a gap of 7 μm, and a pillar height of 40 μm. The geometry for this array is shown in Fig. 4. A symmetry plane is used so that only the top half of the array is simulated. Fig. 4c) highlights the necessary modification to the N^{th} lateral gap. If this lateral gap is not modified, Eq. (1) and Eq. (2) indicate that the 8^{th} gap must have a width of 15.8 μm. By increasing the width of the adjacent lateral gap by 2 μm, the

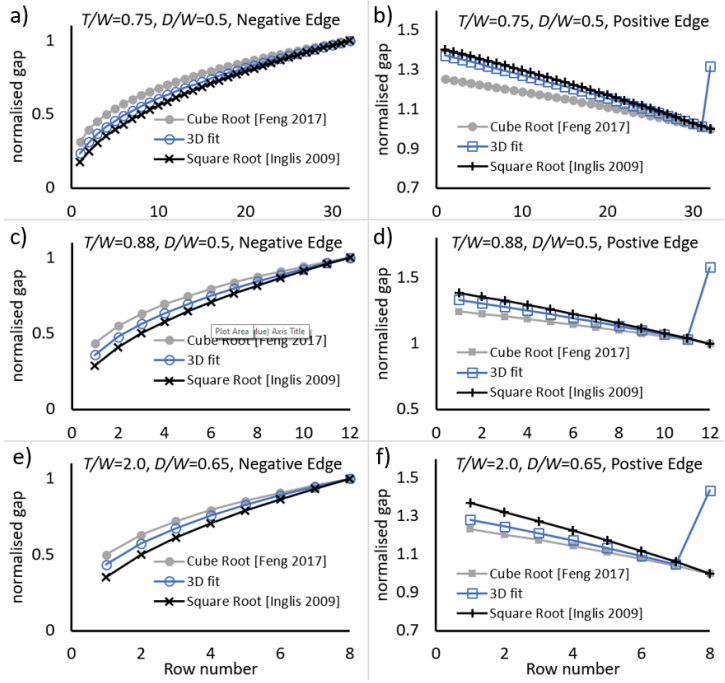

Fig. 3 Normalised gaps along negative and positive edges for three example DLD designs (all lengths in microns): a)/b) $N = 32$, $D = 20$, $W = L = 40$, $T = 30$, N^{th} lateral gap = 29. c)/d) $N = 12$, $D_{\text{axial}} = 23$, $D_{\text{lat}} = 20$, $W = L = 40$, $T = 35$, N^{th} lateral gap = 22. e)/f) $N = 8$, $D = 13$, $W = L = 20$, $T = 40$, N^{th} lateral gap = 9.

8^{th} boundary gap can have a more reasonable width of 10 μm or 1.43 times the bulk gap.

For the design shown in Fig. 3a) and b), where $\varepsilon = 1/32$, we must widen the N^{th} lateral gap. Without modification, Eq. (1) and Eq. (2) require the 32^{nd} positive gap to be more than 13 times wider than the bulk gap. This geometry is impractical to draw, and would be outside the valid range for the model. For example D/W for this gap would be less than 0.08, but the valid range is $0.3 \leq D/W \leq 0.9$.

At the N^{th} positive boundary, the sum of R_N^+ and $R_{N,\text{lat}}^+$ is fixed, but the individual values should be adjusted to make a reasonable layout and stay within the model's range. A MATLAB function (and stand-alone GUI) that calculates the boundary gaps based on user input parameters is available for download in the supplementary material and from the corresponding author.

5 Results

To validate the design process described above, we have simulated the two smaller designs ($N = 12$ and $N = 8$) shown in Fig. 3 using COMSOL 3.5a. One of these simulations is shown in Fig. 4. A typical simulation domain has 100,000 mesh ele-

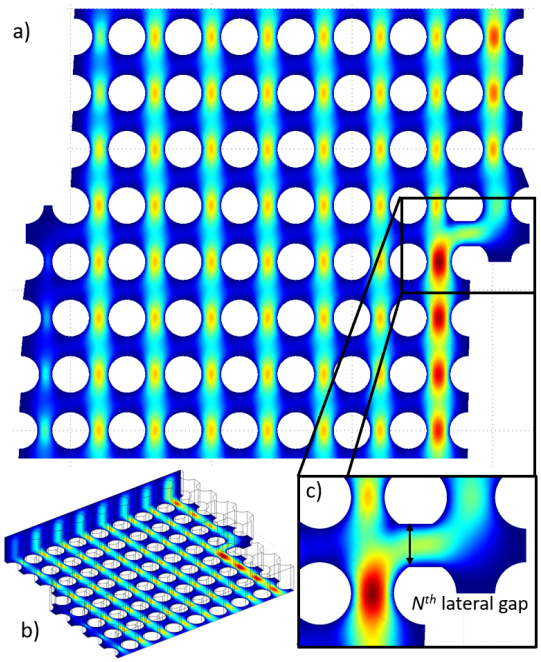

Fig. 4 The design and simulation results from Fig. 3e)/f). The inlet and outlet are linked by periodic boundary conditions. Flow is driven by a body force at a slope of 1/8, Re $\ll 1$. a) The flow field at the mirror symmetry plane (mid height). b) Orthogonal view of simulation domain. c) Detail view of N^{th} gap on positive boundary showing how the resistance of the lateral gap is reduced.

ments and takes about 3 minutes to solve on a modest laptop (Intel Core i7-6600U @ 2.60GHz) with 8 GB of memory.

We make two measurements to quantify the success of the new method (Fig. 5). First, we integrate the flux moving laterally into (or out of) the boundary-adjacent column at each row. In a perfect solution this should be equal to ε times the flux passing through a gap in the forward direction. For the 1/12 array it should be 8.33%, and for the 1/8 array it should be 12.5%. This is shown as a horizontal dashed line in Fig. 5a and b. We can achieve mesh invariance for this measurement with a uniform meshing scheme.

For the second measurement in Fig. 5, we determine the width of the first flow-lane (β) for each row at the positive and negative boundaries. Mesh invariance for this measurement requires a coarse mesh throughout the array with a highly refined mesh around the stall line of interest. The flow-lane width is measured in the gap at the mid-depth (symmetry plane) and near the floor or ceiling (75 or 80% of the pillar depth). The flow-lane width corresponding to a 2D quadratic flow profile is shown with a horizontal dash-dot line.

The results are satisfactory, though the positive boundary shows a too large critical size just before the last row. The critical size at the first gap on the negative boundary is also slightly too large. Fig. 5a) and b) show additional data from designs where the boundary gap is given by the square root of the target flux. This method

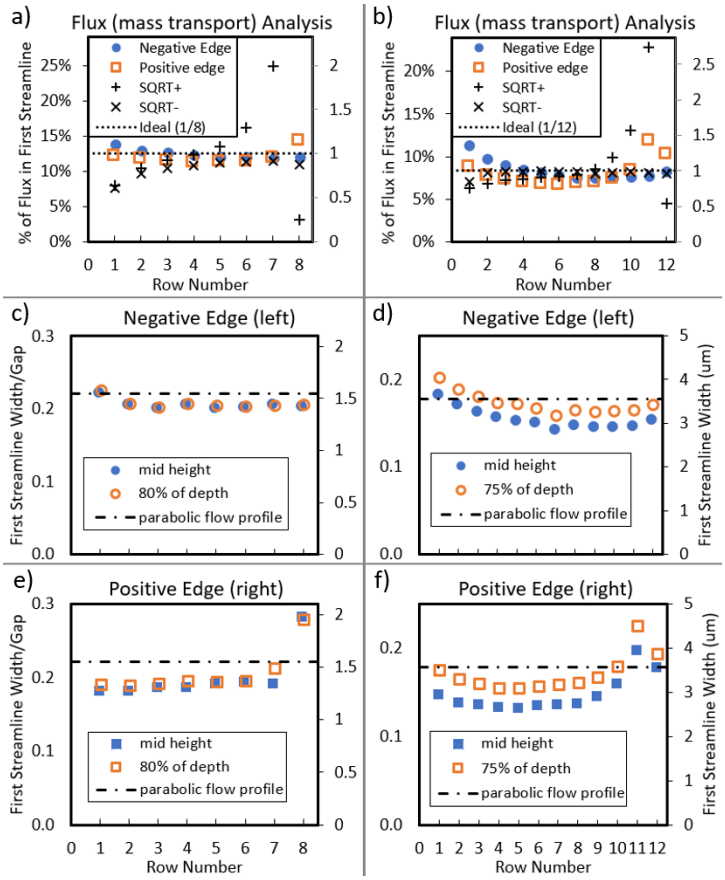

Fig. 5 Analysis of flow pattern and streamline positions for two devices detailed in Fig. 3. Left column is for 1/8 array and right column for 1/12 array. a) and b) show the mass transport of the first flow-lane at each boundary-adjacent gap. The ideal value is shown with a dotted horizontal line. The flux patterns for devices created using the square-root rule are shown as black crosses. c)–f) show the width (normalised, and in μm) of the first flow-lane (β) at the mid-plane and near the lid/floor.

gives a consistent critical size along the negative boundary of the thin 1/12 array (Fig. 5b, '$\times$'), but the critical size is non-uniform along the positive boundaries of both example designs (Fig. 5b, '+').

We find that the width of the first flow-lane is larger near the floor/ceiling, with a more pronounced difference for the device with shorter pillars (Fig. 5d, f). This is consistent with Biagioni et al (2019) who found a slight increase in the first flow-lane width at a plane near the floor or ceiling. Some variation in flow-lane width is likely unavoidable, indicating that a perfect boundary (one that has the same flow-lane width at all locations) is impossible.

6 Conclusion

This work addresses a known problem in DLD separation devices—the disturbance to flow patterns and critical size in the vicinity of array boundaries. A handful of papers have sought solutions using 2-dimensional flow models. Here we use a more complete model of the DLD array that includes forward and lateral fluidic resistance, then use 3-dimensional flow simulations to create a boundary solution that is valid over typical post size and height.

This work makes two significant contributions: 1) it provides a relatively simple model for the resistance of a microfluidic pillar at low Reynolds number. This has obvious utility here, but is also useful for determining the device-level resistance and throughput of microfluidic devices. 2) It provides an improved solution to the DLD boundary problem. Most notably it shows that the N^{th} gap on the positive boundary must be large. The solution will provide better particle separation performance near the DLD boundaries. This is important for narrow devices with small numbers of columns. Narrow devices are critical in efforts to increase volume throughput though parallelisation (Campos-Gonzalez et al, 2018).

Acknowledgements We thank Alison Skelley, Weibin Liang, and James Sturm for helpful discussions about the DLD boundary problem. This work is supported by the Australian Research Council (DP160103442).

A Supplementary Material

'D_Boundaries.m.txt' is a Matlab function that takes inputs of pitch, post size, post height (depth), and returns the boundary gaps as per the method described in this paper. A stand-alone graphical user interface (GUI) to perform the same task without Matlab is available from the corresponding author.

References

Biagioni V, Adrover A, Cerbelli S (2019) On the Three-Dimensional Structure of the Flow through Deterministic Lateral Displacement Devices and Its Effects on Particle Separation. Processes 7(8):498, DOI 10.3390/pr7080498

Campos-Gonzalez R, Skelley AM, Gandhi K, Inglis DW, Sturm JC, Civin CI, Ward T (2018) Deterministic Lateral Displacement: The Next-Generation CAR T-Cell Processing? Slas Technology 23(4):338–351, DOI 10.1177/2472630317751214

Doyeux V, Podgorski T, Peponas S, Ismail M, Coupier G (2011) Spheres in the vicinity of a bifurcation: Elucidating the Zweifach–Fung effect. Journal of Fluid Mechanics 674:359–388, DOI 10.1017/S0022112010006567

Ebadi A, Farshchi Heydari MJ, Toutouni R, Chaichypour B, Fathipour M, Jafari K (2019) Efficient paradigm to enhance particle separation in deterministic lateral displacement arrays. SN Applied Sciences 1(10):1184, DOI 10.1007/s42452-019-1064-5

Feng S, Skelley AM, Anwer AG, Liu G, Inglis DW (2017) Maximizing particle concentration in deterministic lateral displacement arrays. Biomicrofluidics 11(2):024,121, DOI 10.1063/1.4981014

Gleghorn JP, Pratt ED, Denning D, Liu H, Bander NH, Tagawa ST, Nanus DM, Giannakakou PA, Kirby BJ (2010) Capture of circulating tumor cells from whole blood of prostate cancer patients using geometrically enhanced differential immunocapture (GEDI) and a prostate-specific antibody. Lab on a Chip 10(1):27–29, DOI 10.1039/B917959C

Gunda NSK, Joseph J, Tamayol A, Akbari M, Mitra SK (2013) Measurement of pressure drop and flow resistance in microchannels with integrated micropillars. Microfluidics and Nanofluidics 14(3):711–721, DOI 10.1007/s10404-012-1089-1

Huang LR, Cox EC, Austin RH, Sturm JC (2004) Continuous particle separation through deterministic lateral displacement. Science 304(5673):987–990, DOI 10.1126/science.1094567

Inglis DW (2009) Efficient microfluidic particle separation arrays. Applied Physics Letters 94(1):013,510, DOI 10.1063/1.3068750

Inglis DW, Davis JA, Austin RH, Sturm JC (2006) Critical particle size for fractionation by deterministic lateral displacement. Lab on a Chip 6(5):655–658, DOI 10.1039/b515371a

Krüger T, Kusumaatmaja H, Kuzmin A, Shardt O, Silva G, Viggen EM (2017) Lattice Boltzmann Method: Principles and Practice. Lattice Boltzmann Method: Principles and Practice pp 1–694, DOI 10.1007/978-3-319-44649-3

McGrath J, Jimenez M, Bridle H (2014) Deterministic lateral displacement for particle separation: A review. Lab on a Chip 14(21):4139–4158, DOI 10.1039/c4lc00939h

Nagrath S, Sequist LV, Maheswaran S, Bell DW, Irimia D, Ulkus L, Smith MR, Kwak EL, Digumarthy S, Muzikansky A, Ryan P, Balis UJ, Tompkins RG, Haber DA, Toner M (2007) Isolation of rare circulating tumour cells in cancer patients by microchip technology. Nature 450(7173):1235–1239, DOI 10.1038/nature06385

Pariset E, Pudda C, Boizot F, Verplanck N, Berthier J, Thuaire A, Agache V (2017) Anticipating Cutoff Diameters in Deterministic Lateral Displacement (DLD) Microfluidic Devices for an Optimized Particle Separation. Small 13(37):1701,901, DOI 10.1002/smll.201701901

Salafi T, Zhang Y, Zhang Y (2019) A Review on Deterministic Lateral Displacement for Particle Separation and Detection. Nano-Micro Letters 11(1):77, DOI 10.1007/s40820-019-0308-7

Vernekar R, Krüger T, Loutherback K, Morton K, Inglis DW (2017) Anisotropic permeability in deterministic lateral displacement arrays. Lab on a Chip 17(19):3318–3330, DOI 10.1039/C7LC00785J

Zeming KK, Salafi T, Chen CH, Zhang Y (2016) Asymmetrical Deterministic Lateral Displacement Gaps for Dual Functions of Enhanced Separation and Throughput of Red Blood Cells. Scientific Reports 6:22,934, DOI 10.1038/srep22934